Microporous and Mesoporous Materials 284 (2019) 177–185

Contents lists available at ScienceDirect

Microporous and Mesoporous Materials

journal homepage: www.elsevier.com/locate/micromeso

Ultrasensitive sensor based on novel bismuth carbon nanomaterial for lead and cadmium determination in natural water, contaminated soil and human plasma

Zhuotong Zeng[a,1], Siyuan Fang[b,1], Ding Tang[c], Rong Xiao[a,*], Lin Tang[a,b,**], Bo Peng[b], Jilai Gong[b], Beiqing Long[b], Xilian Ouyang[b], Guangming Zeng[a,b]

[a] Department of Dermatology, Second Xiangya Hospital, Central South University, Changsha, 410011, Hunan, China
[b] College of Environmental Science and Engineering, Hunan University and Key Laboratory of Environmental Biology and Pollution Control (Hunan University), Ministry of Education, Changsha, 410082, China
[c] General Surgery, The Third Hospital of Changsha, Changsha 410015, Hunan, China

ARTICLE INFO

Keywords:
Bi_2O_3
Hollow spherical
Ordered mesoporous carbon
Electrochemical sensor
Multipath detection

ABSTRACT

Heavy metals are ubiquitous in the environment, and their excessive discharge and bioaccumulation can cause cardio-vascular and urinary diseases in humans. Among them, lead ion (Pb^{2+}) and cadmium ions (Cd^{2+}) are designated as the most typical toxic metal ions in human blood and drinking water. Thus, high-performance monitoring of $Pb^{2+}$and Cd^{2+} pollution is necessary. Nanomaterials have been extensively used in electrochemical sensing due to their excellent physicochemical properties. In this study, we prepared ordered mesoporous carbon doped hollow spherical bismuth oxide nanocomposites (hsBi_2O_3-OMC NCs), and constructed it into an electrochemical sensor for highly sensitive and specific detection of Pb^{2+} and Cd^{2+} in environmental media and human blood based on the differential pulse anodic stripping voltammetry (DPASV). The experimental results demonstrate that the detection range could be broadened to 200 nM with detection limits of 0.025 nM for Pb^{2+} and 0.045 nM for Cd^{2+}. Compared with conventional detection techniques, this sensor exhibited simple operation, minimal background interference, multipath applicability and economic efficiency. Therefore, we believe that this work is significant for pollution monitoring, environmental restoration and emergency treatment.

1. Introduction

Heavy metals (HMs) pose an increasing threat to ecological safety and public health due to their toxicity which can be greatly amplified by the accumulation of organisms through the food chain [1]. Lead ion (Pb^{2+}) and cadmium ion (Cd^{2+}) act as the most notorious pollutants in human blood, as they can cause severe plastic anemia, musculoskeletal, urinary and cardiovascular diseases. Numerous epidemiological studies observed that these adverse effects are associated with three exposure routes: breathing, eating and skin contact [2,3]. Although discharge of HMs from industry has been extensively controlled in recent years, many sites in Hunan Province are still seriously polluted due to numerous non-ferrous metal mineral resources. The level of HMs in the river sediment and wetland soil is high, especially in the Xiangjiang River Basin, causing great harm to surrounding residents. Therefore, it is significant to develop convenient detection methods for extensive investigation of Pb^{2+} and Cd^{2+} levels in natural water, soil and human blood in contaminated regions. The most common detection techniques, such as graphite furnace atomic absorption spectrometry (GF-AAS), atomic fluorescence spectrometry (AFS), and inductivity coupled plasma atomic emission spectrometry (ICP-AES), are based on the element's intrinsic physical properties [4–6]. However, these methods usually require large-scale instruments, tedious pretreatment process, and excessively high detection limit, which is not conducive to the detection of ultra-trace concentrations in human blood. Hence, the development of universally applicable detection technology for Pb^{2+} and Cd^{2+} quantification in environmental media and human blood with high selectivity and sensitivity is paramount to contaminate

* Corresponding author.
** Corresponding author. Department of Dermatology, Second Xiangya Hospital, Central South University, Changsha, 410011, Hunan, China.
E-mail addresses: xiaorong65@csu.edu.cn (R. Xiao), tanglin@hnu.edu.cn (L. Tang).
[1] These authors contribute equally to this article.

https://doi.org/10.1016/j.micromeso.2019.04.045
Received 28 November 2018; Received in revised form 28 March 2019; Accepted 19 April 2019
Available online 20 April 2019
1387-1811/

regions spanning the globe.

Recently, differential pulse anodic stripping voltammetry (DPASV) has received scientific attention on trace heavy metal determination in human blood and environmental media owing to their high anti-interference ability, effective pretreatment step and fast response time. However, traditional construction methods of bismuth electrodes for DPASV detection, including in-situ/ex-situ depositing bismuth film at an electrode surface [7,8], or drop-casting pre-synthesized bismuth solution on the electrode surface [9], displayed limited sensitivity, and the additional processing step hindered the real-time performance of on-site detection. To overcome these drawbacks, many efforts have been devoted to the design of high-performance electrochemical sensor that is applied to new electrode nanomaterials, which had ultra-high peak signal-to-noise ratio, strong biocompatibility and excellent physicochemical properties.

Hollow materials, such as metallic oxides [10], mesoporous materials [11], and bimetallic composites [12], have attracted much attention in electrochemical sensing field. For example, Liu et al. [13] fabricated a mediator-free biosensor to immobilize hemoglobin through hollow titanium dioxide modified rGO microspheres. Xiong and his coworkers also prepared an original electrochemical sensor to distinguish homologues and isomers based on hollow mesoporous silica spheres [14]. Inspired by the above work, we found that hollow spherical bismuth oxide ($hsBi_2O_3$), benefiting from its good electrical conductivity and thermal properties, has a great potential for applications in the electrochemical sensing. Moreover, our previous work has proven that ordered mesoporous carbon (OMC) with extremely ordered structural integrity and uniform pore consistency are more suitable as a spring board when applied in electrochemical analysis [15,16]. Secondly, compared with activated carbon or bio-char, OMC has much-improved interface load ratio and conductivity because of its high surface area, abundant and high-density groups and regular meso-structure. Finally, OMC-metal oxide nanocomposites can achieve integrated performance with synergistic effects in environmental monitoring and clinical diagnosis because of their excellent biocompatibility and facile regulation [17,18].

Herein, an integrated ordered mesoporous carbon doped hollow spherical bismuth oxide nanocomposites ($hsBi_2O_3$-OMC NCs) was developed, optimized and validated in real samples. The $hsBi_2O_3$-OMC NCs enlarged active surface area and high conductivity, more electroactive sites, diffusion resistance minimization and excellent biocompatibility. Additionally, this sensor showed outstanding performance with a good linear range of 0.50–200 nM, lower detection limits of 0.025 nM and 0.045 nM to Pb^{2+} and Cd^{2+}, respectively. More importantly, this strategy affords a simple, sensitive and universal platform for detection of HMs in both human blood and environmental media.

2. Experimental

2.1. Materials and measurements

Pluronic copolymer (P123, Sigma-Aldrich). Tetraethoxysilane (TEOS), Furfuryl alcohol, Chitosan ($(C_6H_{11}NO_4)_n$), Bismuth nitrate ($Bi(NO_3)_3{\cdot}5H_2O$), Cadmium nitrate ($Cd(NO_3)_3{\cdot}4H_2O$), and Lead nitrate ($Pb(NO_3)_2$) (Macklin Biochemical Co., Ltd. China). All the working solutions were stepwise diluted stock solution (1.0 μM $Cd(NO_3)_2$ or $Pb(NO_3)_2$) and stored at 4 °C for further use. Supporting electrolyte (0.10 M, pH 4.5) was prepared by CH_3COOH and CH_3COONa. Milli-Q water (18.2 MΩ cm^{-1}, Millipore) was used throughout the experiment. All chemicals were analytical grade.

Transmission electron microscopy (TEM) and Field emission scanning electron microscopy (FESEM) were performed with a FEI Tecnai G^2 F20 and a Hitachi S-4800 microscope, respectively. X-ray photoelectron spectroscopy (XPS) was characterized by Kratos XSAM800, and X-ray diffraction (XRD) was analyzed with Bruker D8 Discover using Cu K_α radiation with 40 kV operation voltage from 10° to 80°. The automatic specific surface area and porosity analyzer (JW-BK122W) was determined by the specific surface areas of $hsBi_2O_3$-OMC NCs. Functional groups of the $hsBi_2O_3$-OMC NCs were characterized by Fourier infrared spectrometer (FTIR, Thermo ESCALAB 250XI) using the KBr disk as the background, and the spectra was scanned from 400 to 4000 cm^{-1} with a resolution of 4 cm^{-1}.

2.2. Preparation of $hsBi_2O_3$-OMC NCs

SBA-15 and OMC were synthesized according to our published studies [15,16]. Briefly, 100 mg of as-prepared SBA-15 were soaked with 10 mL of miscible liquids (ethanol and 50 mg oxalic acids). Then, 2 mL of furfuryl alcohol were added to the mixture and stirred until completely dissolved. Next, the solution was placed in the oven at 90 °C for 10 h, and the obtained solid was ground sufficiently and subsequently calcinated at 900 °C for 2 h in a vacuum tube furnace. Finally, 2.0 M NaOH solutions were used to remove silicon template and obtain the OMC material.

Additionally, the $hsBi_2O_3$-OMC NCs were obtained by solvothermal method as follows. Before ultrasonically dispersed to form a homogeneous liquid, 500 mg of OMC and 970 mg of Bi $(NO_3)_3{\cdot}5H_2O$ were dissolved into the mixture solution (30 mL of glycerol and 30 mL of absolute ethanol). Next, the mixed liquor was decanted in inner lining of Teflon reactor, sealed and heated at 160 °C for 5 h. The as-formed precipitate was collected and washed with deionized water for several times after the reactant cooled to room temperature, followed by drying at 60 °C overnight. Finally, the precipitate was calcined in a muffle furnace at 270 °C for 2 h, with a heating rate of 2 °C/min to obtain $hsBi_2O_3$-OMC NCs.

2.3. Fabrication of $hsBi_2O_3$-OMC NCs based electrochemical sensor

Before the modification step, the bare GCE was polished orderly with 1, 0.3 and 0.05 μm alumina slurry, followed by rinsing ultrasonically with acetone, ethanol and ultrapure water, respectively, and finally allowed to dry at ambient temperature. Then, the bare GCE was scanned by cyclic voltammetry in 0.50 M H_2SO_4 between −0.4 V and 0.8 V (vs. SCE) at 100 mV s^{-1} to reach a steady state. Additionally, 15 mg of $hsBi_2O_3$-OMC NCs were dispersed in 10 mL of 0.1 M acetic acid containing 12 mg of chitosan under sonication to form stable and homogeneous suspension. Fabrication of $hsBi_2O_3$-OMC NCs/GCE was carried out and 5.0 μL of $hsBi_2O_3$-OMC NCs suspension were dropped onto the GCE surface by one-step, and left to dry overnight at ambient environment. For comparison, 5.0 μL of OMC suspension were dropped onto the bare GCE surface to fabricate the OMC/GCE.

DPASV experiments were conducted on an electrochemical workstation (CHI760E, CHI Instruments Co., China) with a classical three-electrode system, including a glassy carbon working electrode (modified with $hsBi_2O_3$-OMC NCs), a Pt wire as the counter electrode, and a Hg/HgO electrode as the reference electrode, respectively. The voltammetry measurements of $hsBi_2O_3$-OMC NCs/GCE was performed in 0.1 M supporting electrolyte (pH 4.5, 0.1 M KCl) containing different concentration Pb^{2+} and Cd^{2+}. The following parameters were used for DPASV measurements: step potential 5 mV, frequency 50 Hz, amplitude 25 mV and scan rate 100 mV s^{-1}.

3. Results and discussion

3.1. Characteristic and electrochemical property

Nitrogen adsorption-desorption analysis revealed that $hsBi_2O_3$-OMC NCs had mesoporous structure due to the presence of type-IV isotherm and hysteresis loop (Fig. S1). The specific surface area of $hsBi_2O_3$-OMC NCs is 1505.6 m^2/g, and the pore volume is 2.00 cm^3/g (Table S1), which are in line with other mesoporous materials exhibiting similar

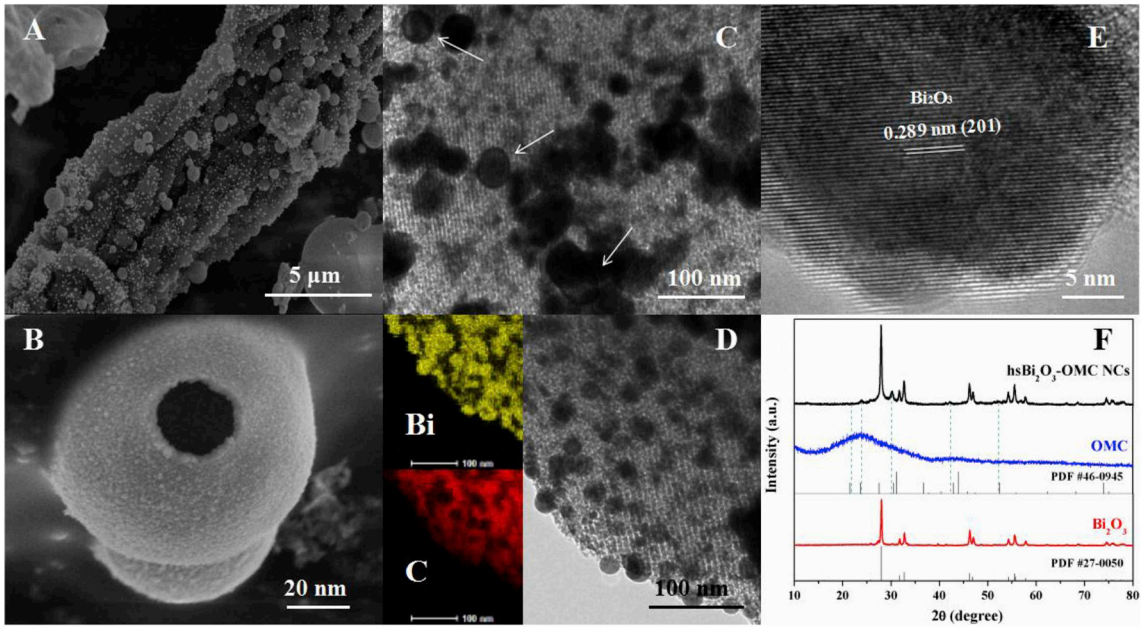

Fig. 1. Characteristics of the as-prepared $hsBi_2O_3$-OMC NCs. (A, B) FESEM images, (C, D) TEM and corresponding EDX mapping. (E) HRTEM image taken from the edge of $hsBi_2O_3$. (F) XRD patterns of $hsBi_2O_3$-OMC NCs compare with Bi_2O_3 and OMC.

pore sizes [19]. The as-prepared $hsBi_2O_3$ were well dispersed with monodisperse nanospheres and hollow structure (Fig. 1A and B). The spring board OMC consists of highly ordered mesoporous arrays with average aperture of 6 nm, and the internal hollow structure of $hsBi_2O_3$ can be confirmed by the appearance of dark edges and transparent interiors based on electron density (Fig. 1C). Besides, the EDX elemental map of $hsBi_2O_3$-OMC NCs indicates that Bi and C are evenly distributed across entire composites where the black part of the bismuth element exactly corresponds to the presence of carbon (Fig. 1D). The lattice fringes of Bi_2O_3 are clearly visible of about 0.289 nm, which are close to the spacing of (201) planes (Fig. 1E), and the relative strong intense peaks at 2θ values of 27.95°, 32.69°, 46.22° are allocated to the crystal planes of Bi_2O_3, which are well indexed to (201), (220) and (222) planes with a = 5.840 Å, b = 8.160 Å and c = 7.490 Å, respectively [20]. While the intense peaks at 21.55°, 23.71°, 30.49°, 43.92° and 52.52° are assigned to the carbon (Fig. 1F).

Additionally, their full range XPS analysis shows Bi 4f, C 1s, and O 1s signals from OMC, Bi_2O_3 and $hsBi_2O_3$-OMC NCs (Fig. S2). The Bi 4f energy peak is divided into two peaks for the Bi_2O_3 due to the existence of Bi^{3+} (Fig. 2A), while the peak at 161.49 eV is due to the strong repulsion between O^{2+} in $hsBi_2O_3$-OMC NCs and the loss of $Bi6^2$ electrons to result in some of Bi^{3+} converted into Bi^{5+} [21]. However, three Bi 4f

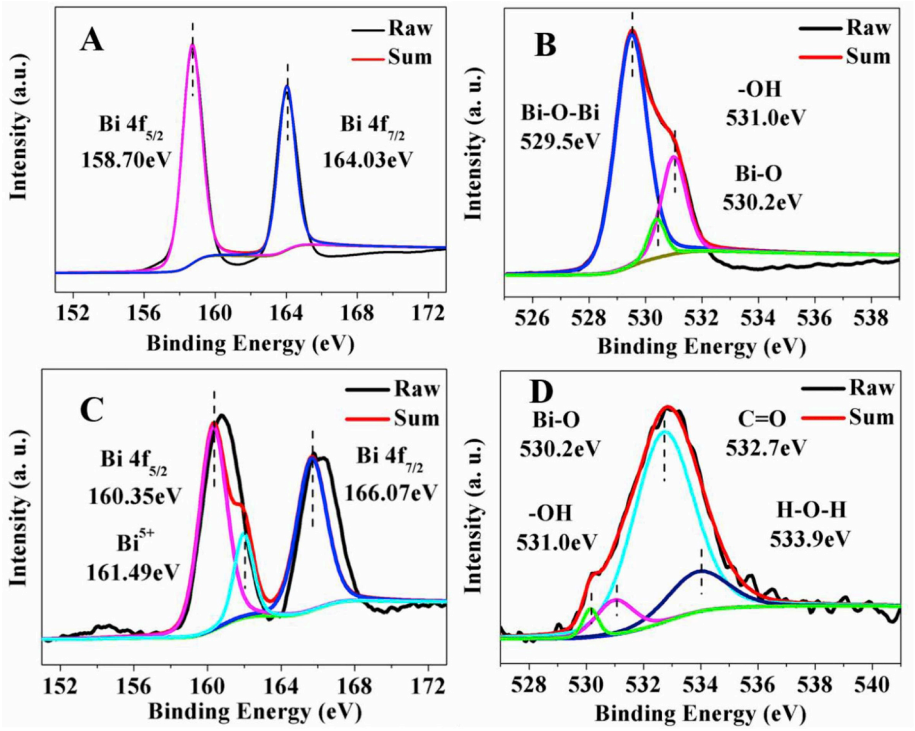

Fig. 2. XPS be peaking spectrograms of Bi4f and O1s in (A, B) Bi_2O_3 and (C, D) $hsBi_2O_3$-OMC NCs.

BE peaks in $hsBi_2O_3$-OMC NCs are noted to move to higher binding energy, because of the strong interaction between $hsBi_2O_3$ and OMC. Furthermore, four binding energy peaks of O 1s are fitted at 530.2 eV, 531.0 eV, 532.7 eV and 533.9 eV in $hsBi_2O_3$-OMC NCs, which should be assigned to Bi—O, —OH, C=O and H—O—H, respectively (Fig. 2D). Moreover, it can be seen from the O 1s peak splitting figure that the higher energy peak is because the oxygen atoms are connected to high electron negative cation and bridging oxygen. While the lower energy peak belongs to the oxygen atoms bonded to low electron negative cation and non-bridging oxygen [22,23].

To confirm the influence of functional groups on the material structure, FTIR results showed that SBA-15 has a strong peak at 1110 cm^{-1} with a small and narrow shoulder at 1180 cm^{-1}, which is relative with the network motions of transverse (TO) and longitudinal (LO). The peak at 802 cm^{-1} corresponds to Si—OH stretching vibration [24,25]. Common peak at 1120 cm^{-1} for OMC and $hsBi_2O_3$-OMC NCs can be assigned to C—O and C—O—C stretching vibrations, and the band at 1586 cm^{-1} is attributed to C=C stretching vibrations, which are the skeleton structure of OMC and its benzene ring in the benzene ring, and 1660 cm^{-1} peak corresponds to C=O or C=C stretching vibrations. Both composite materials also exhibited common peaks appearing at 2274 cm^{-1} and 2361 cm^{-1} corresponding to the Fermi resonance effect between saturated C—H stretching vibration and in-plane bending vibration (Fig. S3).

According to the results presented herein, Scheme 1 describes the sequential stages in the synthesis of $hsBi_2O_3$-OMC NCs, including the formation of ordered mesoporous carbon, the decomposition and evolution of carbon precursor combining the Ostwald ripening and self-assembly process, and the growth of $hsBi_2O_3$ NCs spherical structures [26]. We proposed that the formation of $hsBi_2O_3$-OMC architecture could be formulated as follows [Eqs. (1) and (2)]:

$$Bi(NO_3)?5H_2O + HOCH_2CHOHCH_2OH + 3C_2H_5OH \rightarrow Bi(CH_2-CHO-CH_2O) + 3C_2H_5ONO_2 + 8H_2O \quad (1)$$

$$2Bi(CH_2\,O-CHO-CH_2O) + 3H_2O \rightarrow Bi_2O_3\downarrow + 2HOCH_2CHOHCH_2OH \quad (2)$$

During this process, carbon acted as a spring board allowing these bismuth particles to converge and form the center of the particles. Owing to their higher surface energy, the nano building dissolved and diffused to the external surface of this structure, thus forming a hollow spherical structure, and then hydrolyzed in the intermediate Bi (CH_2O—CHO—CH_2O) at 270 °C calcination to form porous Bi_2O_3 spheres [20]. The $hsBi_2O_3$-OMC NCs used for electrochemical sensing have changed the traditional method of bismuth film or extra-additional bismuth composite in previous reports. The use of one-step dropping method to prepare the electrode greatly saves time, simplifies cumbersome procedures, reduces interference, and increases sensitivity.

3.2. Characteristics of $hsBi_2O_3$-OMC NCs-based electrochemical sensor

The cyclic voltammogram (CV) and electrochemical impedance spectroscopy (EIS) were used as powerful tools to determine the interfacial properties and impedance changes in the electrode modification process. In this process, $Fe[(CN)_6]^{3-/4-}$ as electrolyte and their redox current at the bare GCE was poor, which had quasi-reversible one-electron redox behavior with peak potential separation (ΔE_p) of 0.166 V. While OMC or $hsBi_2O_3$-OMC NCs were modified on GCE, the redox peaks gradually increased and the ΔE_p (0.1 V) decreased, implying that $hsBi_2O_3$-OMC NCs/GCE enabled better electron transfer rate and good electrode performance compared to bare GCE and OMC/GCE (Fig. 3A). This result was attributed to the effective electron transfer capacity between $hsBi_2O_3$ and OMC.

The hypothesis was also well supported by the EIS data in which $hsBi_2O_3$-OMC NCs had fast electron transfer kinetics. Nyquist plots (Z′ vs -Z″) of bare GCE showed a large R_{ct} value indicating the slowest electron transfer rate between the bare GCE and $Fe[(CN)_6]^{3-/4-}$ probe. After modification of OMC or $hsBi_2O_3$-OMC NCs on electrode surface, two straight lines were observed, and the R_{ct} values followed the order: $hsBi_2O_3$-OMC NCs/GCE (0.008 Ω) < OMC/GCE (0.010 Ω) < < bare GCE (387.7 Ω) (Fig. 3B, Table S2). It is inferred that $hsBi_2O_3$-OMC NCs have larger effective surface area with more active sites to enhance electroactivity and lead to a higher signal-to-noise ratio. Moreover, the effective surface area (A) of $hsBi_2O_3$-OMC NCs/GCE was calculated as 0.230 cm^2 using Randles-Servick equation [27]. The A value of $hsBi_2O_3$-OMC NCs/GCE was 15.5% larger as compared to that of OMC/GCE,

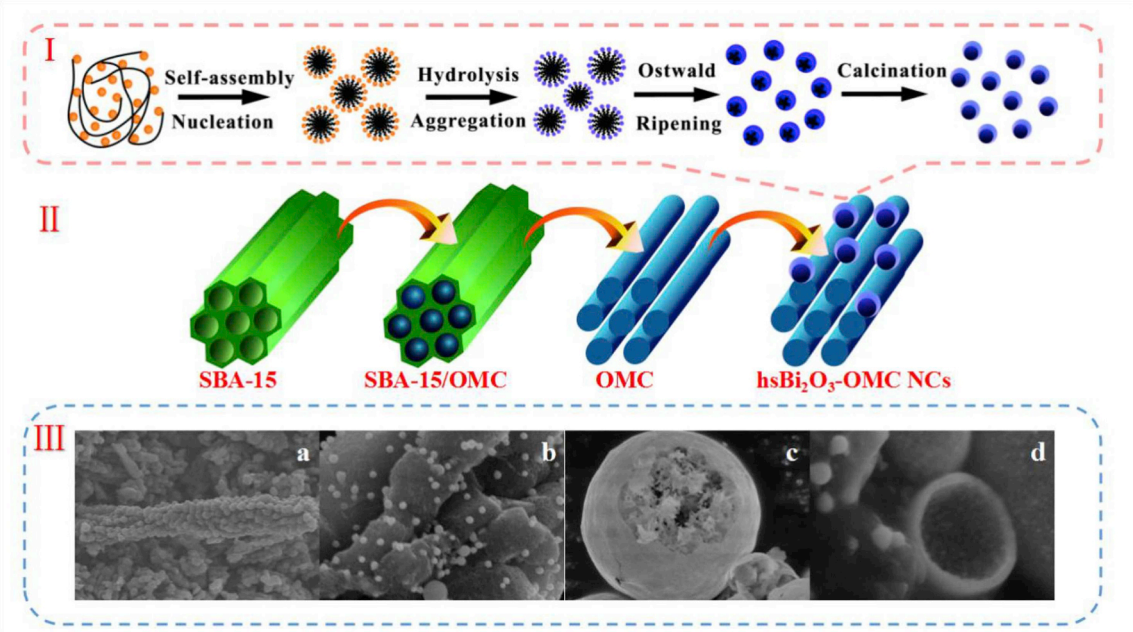

Scheme 1. The formation process of (I) hollow spherical bismuth oxide, (II) mesoporous carbon and $hsBi_2O_3$-OMC NCs, (III) the FESEM images of (a) OMC, (b) $hsBi_2O_3$-OMC NCs, (c) the intermediate morphology after the Ostwald Ripening, (d) the morphology of the calcined$hsBi_2O_3$loaded on OMC.

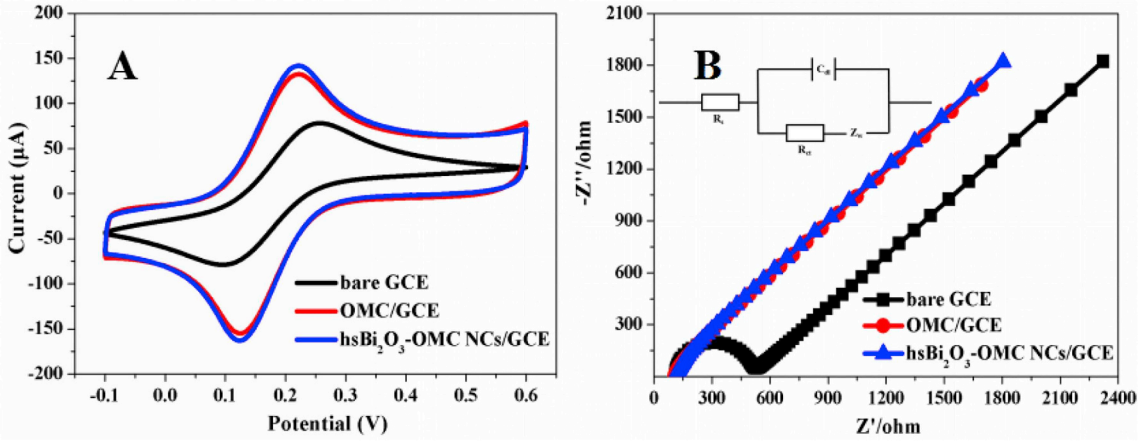

Fig. 3. Comparison of different modified electrodes' electrochemical properties. (A) Cyclic voltamogram (CV) and (B) Electrochemical impedance spectra (EIS) of bare GCE (black), OMC/GCE (red) and $hsBi_2O_3$-OMC NCs/GCE (blue) in 5 mM $Fe(CN)_6^{3-/4-}$ (0.1 M KCl) solution.(insert) Equivalent circuit diagram. Conditions: scan rate: 100 mV s-1, frequency range: 0.01Hzto10kHz. AC amplitude: 5.0 mV. (For interpretation of the references to colour in this figure legend, the reader is referred to the Web version of this article.)

which signified that $hsBi_2O_3$ contributed to the increase in A (Fig. S4).

3.3. Optimization of electrochemical sensing conditions

Some experimental conditions were optimized to achieve the excellent performance of electrochemical sensor for Pb^{2+} and Cd^{2+} determination, including pH (3.0–6.0), drop-cast volume (1.0–11.0 μL), deposition potential (−1.8～-0.8 V) and deposition time (50–300 s). From Fig. 4A, the current is increased (3.0–4.5) and then decreased from 4.5 to 6.0. The possible reason for this phenomenon is that with the addition of chitosan, the functional group is negatively charged and can be used as a cation to promote non-faraday binding effect of metal cation in the preconcentration process, thus promoting the sensitivity of modified electrode surface. When pH is below 4.5, metal cations and hydrogen ions in the solution can undergo ion exchange on the surface of chitosan, binding site competition, and proton interaction with the

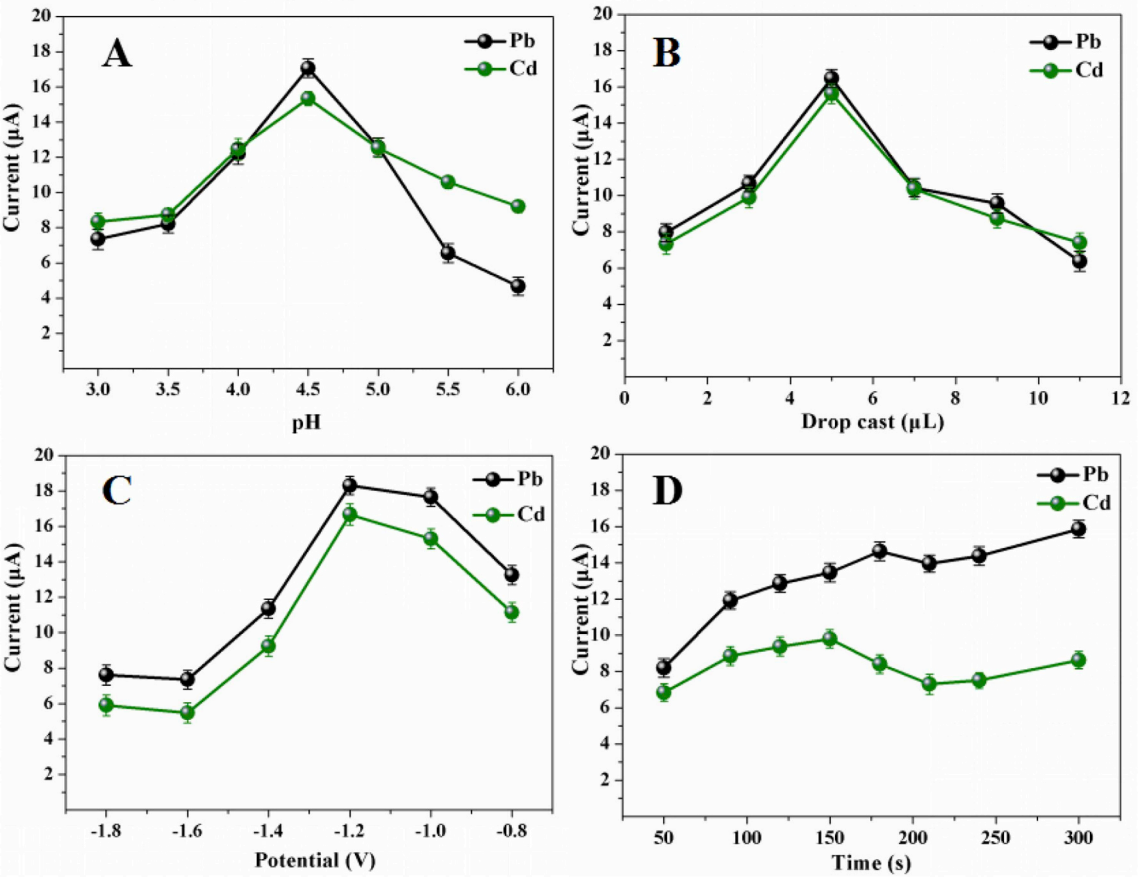

Fig. 4. Effect of experiment conditions in $hsBi_2O_3$-OMC NCs/GCE. (A) pH, (B) drop cast volume, (C) deposition potential, (D) deposition time with 10.0 nM Pb^{2+} and Cd^{2+}. Differential pulse anodic stripping voltammetry (DPASV) recorded at 50 Hz frequency and 25 mV amplitude in 0.1 M acetic buffer solution containing 0.1 M KCl (error bars, n = 3).

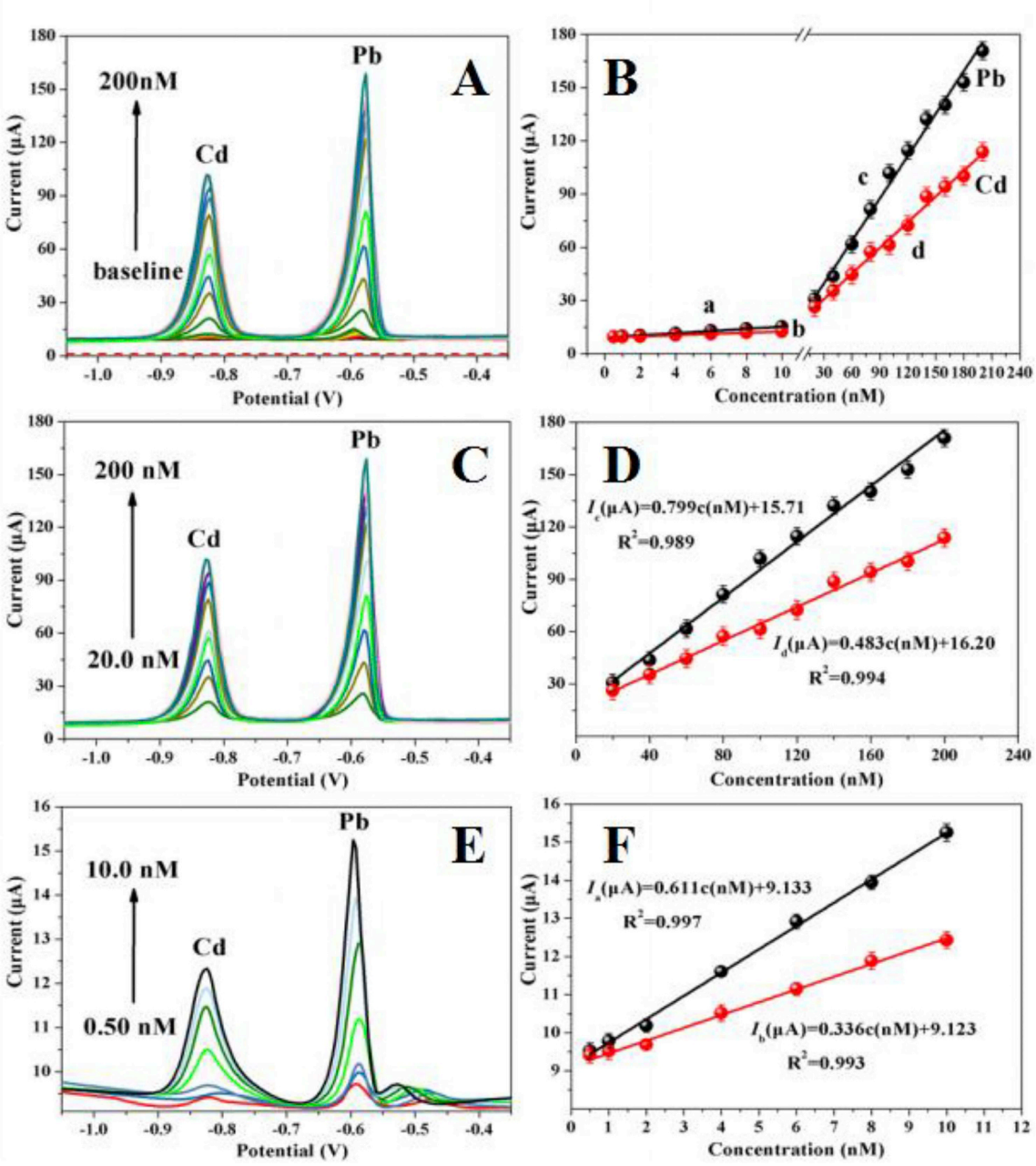

Fig. 5. Simultaneous responses of hsBi_2O_3-OMC NCs of Pb^{2+} and Cd^{2+} determination indifferent ranges. (A, B) baseline to 200 nM, (C, D) 0.5–10.0 nM, and (E, F) 20–200 nM.

surface of mesoporous carbon, resulting in a reduction in peak current. In addition, the hydrolysis on the electrode surface formed bismuth hydroxide, which also reduced the electrochemical active surface area of the modified electrode.

In addition, the peak current of drop-cast volume of hsBi_2O_3-OMC NCs suspension on GCE surface was higher at 5.0 μL, and an obvious decrease in current intensity above 7.0 μL (Fig. 4B) was observed. This may be attributed to the formation of multiple layers of the bismuth film resulting in a higher background current. What's more, the effect of deposition potential was studied from −1.8 V to −0.8 V, and the peak current of Pb^{2+} and Cd^{2+} increases gradually with the increase of deposition potential from −0.8 V ~ −1.2 V until it reaches the maximum at −1.2 V. However, with the increase of deposition potential, overpotential leads to the increase of electron-mediated transfer dynamics, and the co-action of the competitive hydrogen evolution of metal ion hydrolysis on the surface of the modified electrode results in the attenuation of current signal (Fig. 4C). Similarly, despite a brief drop in the current of Cd^{2+}, the slope of the curve got significantly enhanced from 50 s to 300 s (Fig. 4D). Hence deposition potential of −1.2 V and deposition time of 150 s had been chosen for following tests.

3.4. Electrochemical response of hsBi_2O_3-OMC NCs to Pb^{2+} and Cd^{2+}

Under the optimum conditions, two series of well-defined peaks corresponding to Pb^{2+} and Cd^{2+} appeared at about −0.58 V and −0.83 V, respectively. With an increase in the concentration range of 0.50 nM–200 nM, the anodic peak currents shed light on the linearity from 20.0 nM to 200 nM and from 0.50 nM to 10.0 nM (Fig. 5). As a function of concentration, the regression equations can be obtained as follows:

$$I_a(\mu A) = 0.611C_a(nM) + 9.133(R^2 = 0.997) \quad (3)$$

$$I_b(\mu A) = 0.336C_b(nM) + 9.123 \quad (R^2 = 0.993) \quad (4)$$

$$I_c(\mu A) = 0.799C_c(nM) + 15.71(R^2 = 0.989) \quad (5)$$

$$I_d(\mu A) = 0.483C_d(nM) + 16.20(R^2 = 0.994) \quad (6)$$

where, I and C indicate the detection current and heavy metal ions concentration, respectively. The subscripts a, and b represents the Pb^{2+} and Cd^{2+} at low concentration range; c, and d represent the Pb^{2+} and Cd^{2+} at high concentration range.

Although the specific explanation of bilinear ranges in sensing procedure has rarely been discussed in literature, we infer the change in linearity from three aspects, including oxygen functional groups, molecular interaction, and pore structures. Firstly, the oxygen functional groups (−OH, −O−) are activating groups and act as electron donors at the edges and basal planes of carbon, allowing electrons to drift to the mesoporous carbon ring structure to form partially negatively charged species, thereby promoting a large amount of Pb^{2+} and $Cd^{2+}$to attach to the surface of the material and to achieve higher sensitivity at high concentration range [28]. Additionally, FTIR results show that there are functional groups such as C−O, C=O, and C−O−C in hsBi_2O_3-OMC NCs, which affects the dispersion/repulsion interactions between the basal planes and Pb^{2+} and Cd^{2+}. The main reason is that positive holes are generated in the conductive π-band on the graphite carbon surface by locating and removing electrons from the π-electron system on the carbon surface, which could explain the phenomenon at lower concentration range [29].

Secondly, surface structure defects and doping, pore diffusion and collision effects, and spatial effects play a major role in the migration dynamics and sensing detection of heavy metals in porous materials. Because the pore size of the material is concentrated at 2–3 nm, and the average pore diameter is 6 nm, the maximum transport dynamics of Pb^{2+} and Cd^{2+} are associated with the adsorption behavior, and the stochastic flights in pore system mainly controlled the overall kinetics [30]. On the other hand, the occurrence of irreversible capillary condensation in wide mesopores limits the transport rate of metal ions through the pores, resulting in reduced transport kinetics. This assumption can be verified by the presence of type-IV adsorption isotherms and hysteresis loops, which is also an important factor affecting the linear relationship [31].

Finally, the physical adsorption of Pb^{2+} and Cd^{2+} onto hsBi_2O_3-OMC NCs takes place mainly through dispersive interactions (basically in the form of electrostatic interactions) between the metal ions and carbon planes. When the concentration of metal ions is higher and the deposition time is longer, the metal cations can accumulate on the pre-deposited monolayer to form a multilayer composite film, leading to positive anode peak potential and becoming sharp, affecting the relationship between Pb^{2+} and Cd^{2+} concentrations and currents [28].

In addition, the limit of detection (LOD, S/N = 3) of the present Pb^{2+} and Cd^{2+} sensor was calculated to be 0.025 nM and 0.045 nM, respectively, representing the result of Pb^{2+} and Cd^{2+} determination have been improved compared with the reported results (Table S3). Therefore, it can be concluded that hsBi_2O_3-OMC NCs sensor possesses rational linear ranges and an acceptable LOD toward the simultaneous detection of Pb^{2+} and Cd^{2+}.

3.5. Reproducibility, repeatability and sensor stability

The reproducibility was controlled by five hsBi_2O_3-OMC NCs/GCEs in simultaneous detection of 10.0 nM Pb^{2+} and Cd^{2+} under optimized conditions. The results confirmed a good reproducibility with the relative standard deviations (RSD) of the current responses at 2.42% for Pb^{2+} and 2.68% for Cd^{2+}, respectively (Fig. 6A). Similarly, the repeatability was also evaluated with the same solutions for five repetitive measurements at a single hsBi_2O_3-OMC NCs/GCE under the optimized conditions. The RSD of peak currents for five replicated trials were 2.31% for Pb^{2+} and 2.71% for Cd^{2+} (Fig. 6B). These low standard deviations fully prove good results for reproducibility and repeatability of the proposed sensor. In addition, the stability of this sensor was investigated by storing hsBi_2O_3-OMC NCs/GCE in the refrigerator at 4 °C. The electrochemical sensor retained 91.06% and 87.51% of its original response to Pb^{2+} and Cd^{2+} after a month storage (Fig. 6C). Therefore, all the results indicated that the fabrication procedure was credible and the proposed sensor showed accurate detection for Pb^{2+} and Cd^{2+} with minimal concentration, high reproducibility and long-term stability.

3.6. Specificity of the sensor

Anti-interference experiments were mainly conducted to evaluate the sensing performance in the presence of common metal ions that may co-deposit with target metal ions or have a competitive inhibitory effect on the active site. Therefore, some heavy metal was used as interfering species in the 0.1 M acetic buffer solution containing 10.0 nM Pb^{2+} and Cd^{2+} for DPASV analysis under optimum conditions. It can be observed that 100-fold K^+, Zn^{2+} and Ni^{2+}, 50-fold Mn^{2+}, Mg^{2+}, and Fe^{3+} exhibited nearly no interference on the Pb^{2+} and Cd^{2+} determination. Hg^{2+} and Cu^{2+} have a relatively larger impact. A 10-fold concentration ratio of Hg^{2+} and Cu^{2+} presented 7% and 10% peak current decrease. While 5-fold concentration ratio of Cr^{3+} and Al^{3+} resulted in less than 5% peak currents decreases (Fig. 6D). To further explore whether this proposed method could be used in a more complex environment, novel bismuth carbon nanomaterial sensor has been applied to evaluate Pb^{2+} and Cd^{2+} in human plasma samples. As we all know, the concentration ratios of Cu^{2+} and K^+ to Pb^{2+}/Cd^{2+} in human plasma environment exceed 10-fold/100-fold. So, we added 0.1 mg/L Cu^{2+} and 1.0 mg/L K^+ into these certified samples to verify the procedure reasonability. As shown in Fig. S5, the presence of Cu^{2+} and K^+ leads to a decrease in the peak current of Cd^{2+} (75.4%～85.6%), but a lesser effect on the peak current of Pb^{2+} (92.2%～96.0%). When the Pb^{2+} and Cd^{2+} coexist in the samples, the influence of current change is negligible (92.0%～96.0%). Therefore, the proposed sensor has superior anti-interference ability both in the environment and biology samples.

3.7. Detection of $Pb^{2}+$ and Cd^{2+} in natural water, soil and human plasma

To test the sensor for trace sensitivity and versatility, natural water samples were collected from Taozi Lake (Changsha, China) and the Xiangjiang River (Changsha, China), respectively. The water samples were filtered with 0.22 μm membrane to remove the impurities and diluted with 0.1 M acetic buffer solution (pH 4.5, 0.1 M KCl). Contaminated soil samples included wetland soil from the Xiangjiang River and lead slag from Shuikoushan Lead Mine (Hengyang, China), which were digested by microwave dissolution method (HJ 680–2013, China). The experimental results of the real spiked water and soil samples were summarized in Table 1. It could be clearly seen that the spiked recoveries were in the range of 95.7–102.4% and the RSD was lower than 5.1%. Compared with ICP-AES method, the detection results obtained by the hsBi_2O_3-OMC NCs/GCE were in good consistent with that of ICP-AES.

In addition, human plasma samples were collected from the local hospital and centrifuged at 7000 rpm for 20 min to take the static supernatant as subsequent samples. Different concentrations of Pb^{2+} and Cd^{2+} were separately spiked into the diluted human plasma samples, and then the presence of Pb^{2+} and Cd^{2+} was determined through the proposed method. Also, the samples were analyzed by AAS, and the results were summarized in Table S4. During the measurement of these samples, the quantitative recovery ranged from 97.9% to 108.4% for detecting Pb^{2+}, whereas it was 95.9%～105.5% for detecting Cd^{2+}. Meanwhile, the relative standard deviation (RSD) ranged from 1.1% to 3.7% were consistent with that of AAS varied from 1.1% to 3.4%,

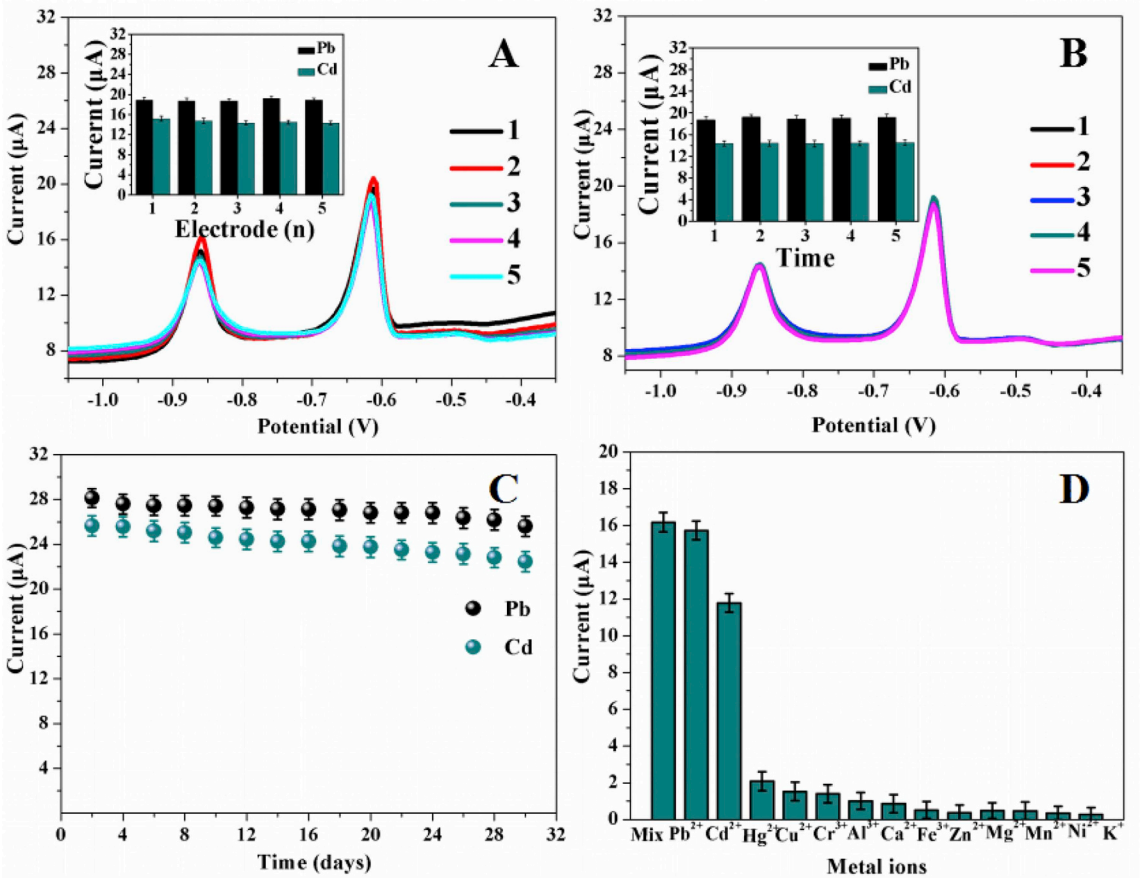

Fig. 6. DPASV measurements of the proposed sensor performance obtained at the $hsBi_2O_3$-OMC NCs/GCE. (A) Reproducibility, (B) repeatability, (C) Stability, (D) Anti-interference ability under optimal experimental conditions. (All the solutions that contained 10.0 nM Pb^{2+} and Cd^{2+}, the error bars indicated standard deviations from three replicative tests.)

Table 1
Determination of Pb^{2+} and Cd^{2+} in environmental samples by the proposed sensor and ICP-AES method (n = 3).

Samples	Original (nM)		Added (nM)		Proposed (nM)		ICP-AES (nM)		Recovery (%)		RSD (%)	
	Pb^{2+}	Cd^{2+}	Pb^{2+}	Cd^{2+}	Pb^{2+}	Cd^{2+}	Pb^{2+}	Cd^{2+}	Pb^{2+}	Cd^{2+}	Pb^{2+}	Cd^{2+}
1	19.31(± 0.23)	–	a	5.00	4.85(± 0.23)	5.12(± 0.15)	4.72(± 0.12)	5.14(± 0.09)	100.4	102.4	1.8	3.3
2	24.13(± 0.19)	–	a	5.00	5.96(± 0.04)	4.94(± 0.21)	5.98(± 0.04)	5.37(± 0.21)	98.70	98.80	3.6	2.9
3	9.65(± 0.12)	–	–	5.00	9.23(± 0.07)	4.86(± 0.14)	9.54(± 0.07)	5.05(± 0.09)	95.70	97.20	2.7	3.2
4	133.8(± 0.26)	177.9(± 0.13)	–	–	132.6(± 0.06)	178.1(± 0.13)	133.1(± 0.18)	178.2(± 0.05)	99.10	100.1	4.3	2.6
5	230.5(± 0.18)	–	b	100.0	116.1(± 0.15)	99.47(± 0.11)	115.9(± 0.09)	100.6(± 0.17)	100.7	99.47	5.1	1.8

[*] 1 = Upstream, 2 = Downstream, 3 = Lake water, 4 = Soil extraction, 5 = Lead mine. [a] The fresh water samples were directly diluted four times with 0.1 M acetic buffer solution (pH = 4.5). [b] The fresh water samples were directly diluted two times with 0.1 M acetic buffer solution (pH = 4.5).

indicating that no significant interference was encountered with the determination of Pb^{2+} and Cd^{2+} in human plasma samples. Therefore, this electrochemical sensor could be utilized to monitor Pb^{2+} and Cd^{2+} levels in environmental and clinical samples.

4. Summary and conclusions

A new method with wide detection range (0.50–200 nM) and excellent selectivity for Pb^{2+} and Cd^{2+} quantification was established by using $hsBi_2O_3$-OMC NCs as electrode material in this work. The detection limits in simultaneous determination of Pb^{2+} and Cd^{2+} were calculated to be 0.025 and 0.045 nM, respectively. Such detection limits were sufficient for Pb^{2+} and Cd^{2+} quantification in surface water with metal concentrations of 0.05 mg/L and 0.005 mg/L, respectively. More importantly, this nanocomposite could be directly used to detect Pb^{2+} and Cd^{2+} in both environmental media and human plasma. We also demonstrated that this excellent detection capability can be correlated to the oxygen functional groups, molecular interaction, and pore structures of the $hsBi_2O_3$-OMC NCs on the glass carbon electrode. This method not only enhanced the electron transfer rate and metal ions load ratio, but also simplified the electrode preparation process, providing a basis of improving the detection sensitivity, selectivity and practicality of the electrochemical sensor. Therefore, this attractive analytical performance makes this electrochemical sensor promising in heavy metal detection in environment and clinical diagnose.

Acknowledgments

The study was financially supported by Projects 81773333, 51579096, 51521006 and 51679084 supported by National Natural Science Foundation of China, the Key Research and Development Program of Hunan Province of China (2017SK2241), the National

Innovative Talent Promotion Program of China (2017RA2088).

Appendix A. Supplementary data

Supplementary data to this article can be found online at https://doi.org/10.1016/j.micromeso.2019.04.045.

References

[1] R. Das, C.D. Vecitis, A. Schulze, B. Cao, A.F. Ismail, X. Lu, J. Chen, S. Ramakrishna, Recent advances in nanomaterials for water protection and monitoring, Chem. Soc. Rev. 46 (2017) 6946–7020.

[2] K. Chen, L. Huang, B. Yan, H. Li, H. Sun, J. Bi, Effect of lead pollution control on environmental and childhood blood lead level in Nantong, China: an interventional study, Environ. Sci. Technol. 48 (2014) 12930–12936.

[3] A. Fang, H. Chen, H. Li, M. Liu, Y. Zhang, S. Yao, Glutathione regulation-based dual-functional upconversion sensing-platform for acetylcholinesterase activity and cadmium ions, Biosens. Bioelectron. 87 (2017) 545–551.

[4] M.A. Qayyum, M.H. Shah, Study of trace metal imbalances in the blood, scalp hair and nails of oral cancer patients from Pakistan, Sci. Total Environ. 593–594 (2017) 191–201.

[5] T.T. Shih, C.C. Hsieh, Y.T. Luo, Y.A. Su, P.H. Chen, Y.C. Chuang, Y.C. Sun, A high-throughput solid-phase extraction microchip combined with inductively coupled plasma-mass spectrometry for rapid determination of trace heavy metals in natural water, Anal. Chim. Acta 140 (2014) 600–608.

[6] G.L. Scheffler, Y. Makonnen, D. Pozebon, D. Beauchemin, Solid sampling analysis of a Mg alloy using electrothermal vaporization inductively coupled plasma optical emission spectrometry, J. Anal. At. Spectrom. 32 (2017) 2041–2045.

[7] L. Shi, Y. Li, X. Rong, Y. Wang, S. Ding, Facile fabrication of a novel 3D graphene framework/Bi nanoparticle film for ultrasensitive electrochemical assays of heavy metal ions, Anal. Chim. Acta 968 (2017) 21–29.

[8] L. Xiao, H. Xu, S. Zhou, T. Song, H. Wang, S. Li, W. Gan, Q. Yuan, Simultaneous detection of Cd(II) and Pb(II) by differential pulse anodic stripping voltammetry at a nitrogen-doped microporous carbon/Nafion/bismuth-film electrode, Electrochim. Acta 143 (2014) 143–151.

[9] M.A. Rico, M. Olivares-Marin, E.P. Gil, Modification of carbon screen-printed electrodes by adsorption of chemically synthesized Bi nanoparticles for the voltammetric stripping detection of Zn(II), Cd(II) and Pb(II), Talanta 80 (2009) 631–635.

[10] C. Cheng, Y. Huang, N. Wang, T. Jiang, S. Hu, B. Zheng, H. Yuan, D. Xiao, Facile fabrication of Mn2O3 nanoparticle-assembled hierarchical hollow spheres and their sensing for hydrogen peroxide, ACS Appl. Mater. Interfaces 7 (2015) 9526–9533.

[11] F.T. Andón, S.P. Mukherjee, I. Gessner, L. Wortmann, L. Xiao, K. Hultenby, A.A. Shvedova, S. Mathur, B. Fadeel, Hollow carbon spheres trigger inflammasome-dependent IL-1β secretion in macrophages, Carbon 113 (2017) 243–251.

[12] H.M. Jeong, J.H. Kim, S.Y. Jeong, C.H. Kwak, J.H. Lee, Co_3O_4-SnO_2 hollow heteronanostructures: facile control of gas selectivity by compositional tuning of sensing materials via galvanic replacement, ACS Appl. Mater. Interfaces 8 (2016) 7877–7883.

[13] H. Liu, K. Guo, C. Duan, X. Dong, J. Gao, Hollow TiO2 modified reduced graphene oxide microspheres encapsulating hemoglobin for a mediator-free biosensor, Biosens. Bioelectron. 87 (2017) 473–479.

[14] C. Xiong, J. Zhao, L. Wang, H. Geng, H. Xu, Y. Li, Trace detection of homologues and isomers based on hollow mesoporous silica sphere photonic crystals, Mater. Horiz. 4 (2017) 862–868.

[15] L. Tang, J. Chen, G. Zeng, Y. Zhu, Y. Zhang, Y. Zhou, X. Xie, G. Yang, S. Zhang, Ordered mesoporous carbon and thiolated polyaniline modified electrode for simultaneous determination of cadmium(II) and lead(II) by anodic stripping voltammetry, Electroanalysis 26 (2014) 2283–2291.

[16] L. Tang, X. Xie, Y. Zhou, G. Zeng, J. Tang, Y. Wu, B. Long, B. Peng, J. Zhu, A reusable electrochemical biosensor for highly sensitive detection of mercury ions with an anionic intercalator supported on ordered mesoporous carbon/self-doped polyaniline nanofibers platform, Biochem. Eng. J. 117 (2017) 7–14.

[17] L. Tang, Y. Zhou, G. Zeng, Z. Li, Y. Liu, Y. Zhang, G. Chen, G. Yang, X. Lei, M. Wu, A tyrosinase biosensor based on ordered mesoporous carbon-Au/L-lysine/Au nanoparticles for simultaneous determination of hydroquinone and catechol, Analyst 138 (2013) 3552–3560.

[18] Y. Zhou, L. Tang, G. Zeng, C. Zhang, X. Xie, Y. Liu, J. Wang, J. Tang, Y. Zhang, Y. Deng, Label free detection of lead using impedimetric sensor based on ordered mesoporous carbon-gold nanoparticles and DNAzyme catalytic beacons, Talanta 146 (2016) 641–647.

[19] G. Yang, L. Tang, G. Zeng, Y. Cai, J. Tang, Y. Pang, Y. Zhou, Y. Liu, J. Wang, S. Zhang, W. Xiong, Simultaneous removal of lead and phenol contamination from water by nitrogen-functionalized magnetic ordered mesoporous carbon, Chem. Eng. J. 259 (2015) 854–864.

[20] Y. Yan, Z. Zhou, Y. Cheng, L. Qiu, C. Gao, J. Zhou, Template-free fabrication of α- and β-Bi2O3 hollow spheres and their visible light photocatalytic activity for water purification, J. Alloy. Comp. 605 (2014) 102–108.

[21] Y. Peng, K.K. Wang, T. Liu, J. Xu, B.G. Xu, Synthesis of one-dimensional Bi_2O_3-$Bi_2O_{2.33}$ heterojunctions with high interface quality for enhanced visible light photocatalysis in degradation of high-concentration phenol and MO dyes, Appl. Catal., B 203 (2017) 946–954.

[22] Y. Wang, Y. Liu, K. Wang, S. Song, P. Tsiakaras, H. Liu, Preparation and characterization of a novel KOH activated graphite felt cathode for the electro-Fenton process, Appl. Catal., B 165 (2015) 360–368.

[23] H. Fan, G. Wang, L. Hu, Infrared, Raman and XPS spectroscopic studies of Bi_2O_3–B_2O_3–Ga_2O_3 glasses, Solid State Sci. 11 (2009) 2065–2070.

[24] A. Danon, P.C. Stair, E. Weitz, FTIR study of CO_2 adsorption on amine-grafted SBA-15: elucidation of adsorbed species, J. Phys. Chem. C 115 (2011) 11540–11549.

[25] Y. Zhou, L. Tang, G. Zeng, J. Chen, J. Wang, C. Fan, G. Yang, Y. Zhang, X. Xie, Amplified and selective detection of manganese peroxidase genes based on enzyme-scaffolded-gold nanoclusters and mesoporous carbon nitride, Biosens. Bioelectron. 65 (2015) 382–389.

[26] Y. Wang, S. Li, X. Xing, F. Huang, Y. Shen, A. Xie, X. Wang, J. Zhang, Self-assembled 3D flowerlike hierarchical Fe3O4@Bi2O3 core-shell architectures and their enhanced photocatalytic activity under visible light, Chem. Eur J. 17 (2011) 4802–4808.

[27] A.I. Gopalan, N. Muthuchamy, K.P. Lee, A novel bismuth oxychloride-graphene hybrid nanosheets based non-enzymatic photoelectrochemical glucose sensing platform for high performances, Biosens. Bioelectron. 89 (2017) 352–360.

[28] L.J. Kennedy, J.J. Vijaya, G. Sekaran, K. Kayalvizhi, Equilibrium, kinetic and thermodynamic studies on the adsorption of m-cresol onto micro- and mesoporous carbon, J. Hazard Mater. 149 (2007) 134–143.

[29] H. Lv, Z. Teng, C. Wang, G. Wang, Ultra-high sensitive voltammetric sensor modified by largely oxygenous functionalized ultrathin carbon nitride nanosheets for detection of Cu (II), Sensor. Actuator. B Chem. 242 (2017) 897–903.

[30] K.M. Zeinu, H. Hou, B. Liu, X. Yuan, L. Huang, X. Zhu, J. Hu, J. Yang, S. Liang, X. Wu, A novel hollow sphere bismuth oxide doped mesoporous carbon nanocomposite material derived from sustainable biomass for picomolar electrochemical detection of lead and cadmium, J. Mater. Chem. 4 (2016) 13967–13979.

[31] D. Saha, S. Barakat, S.E. Van Bramer, K.A. Nelson, D.K. Hensley, J. Chen, Noncompetitive and competitive adsorption of heavy metals in sulfur-functionalized ordered mesoporous carbon, ACS Appl. Mater. Interfaces 8 (2016) 34132–34142.